Journal of Energy Storage 111 (2025) 115378

Contents lists available at ScienceDirect

Journal of Energy Storage

journal homepage: www.elsevier.com/locate/est

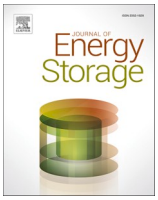

Research papers

Flash rapid synthesis of $Na_3V_2(PO_4)_3$ featured with a nanocrystal/amorphous phase mingled texture for high-rate sodium storage

Liying Hao [a,b,1], Zhikai Li [c,1], Lijuan Cao [d], Haigang Lv [a,*], Yun Zhao [a,b,e,**]

[a] Institute of Molecular Science, Shanxi University, Taiyuan 030006, PR China
[b] Shanxi-Zheda Institute of Advanced Materials and Chemical Engineering, Taiyuan 030006, PR China
[c] State Key Laboratory of Coal Conversion, Institute of Coal Chemistry, Chinese Academy of Sciences, Taiyuan 030001, PR China
[d] Shanxi Key Laboratory of Carbon Materials, National Engineering Laboratory for Carbon Fiber Technology, Institute of Coal Chemistry, Chinese Academy of Sciences, Taiyuan 030001, PR China
[e] Sodium-ion Battery Energy Storage Technology Key Laboratory Cultivation Base Jointly Constructed by the Department and City of Shan Xi Province, Hua Yang Group New Energy Co., Ltd., Yangquan 045000, PR China

ARTICLE INFO

Keywords:
Flash joule heating
$Na_3V_2(PO_4)_3$
Amorphous phase
Pseudocapacitive behavior
Sodium ion battery

ABSTRACT

The sophisticated two-phase transition mechanism of $Na_3V_2(PO_4)_3$ (NVP) cathodes with well-developed crystalline structures always results in diffusion-dominated sodiation/desodiation behaviors and poor rate capability. Herein, by means of a facile flash Joule heating (FJH) process with very short annealing time of 60 s at 1000 °C, a special NVP material (F-NVP/C-1000) featuring with the mingled texture of nanocrystals and amorphous phases is synthesized. Compared to the conventional NVP counterpart fabricating via low-efficient furnace sintering, the intensive nanocrystallization and local amorphous nature together contribute to greatly increased pseudocapacitive charge storage behaviors, which are especially demonstrated by more sloping-type charge/discharge characteristics and some single-phase nonequilibrium Na^+ diffusion. Moreover, the short sintering time and rapid cooling facilitate the distinctly decreased dimension of the as-formed NVP particles, the richer oxygen vacancies in NVP framework and the higher conductivity of F-NVP/C-1000. Systematical kinetics characterizations reveal the F-NVP/C-1000 electrode has much weakened polarization, faster charge transfer and higher ion diffusion rate, helping to achieve substantially enhanced long-term cycling stability upon 2000 cycles and a high reversible capacity of 65.6 mAh g^{-1} at 40C with rate capacity retention of 73.6 %. The results suggest the superb prospective of FJH technologies for developing advanced cathode materials in rechargeable batteries.

1. Introduction

Sodium ion batteries (SIBs) are currently drawing tremendous attention for the applications in large-scale energy storage due to the abundant resource and low cost of sodium salts [1]. Nevertheless, the huger size of Na^+ than Li^+ always causes more evident volume fluctuation and inferior diffusion ability in electrode materials during sodiation/desodiation, incurring greater challenges for maintaining superior cycling stability and rate capability [2,3]. Thus, it is particularly important to exploit appropriate electrode materials when designing high-performance SIBs. At present, the development of satisfactory cathode materials still remains an arduous challenge owing to the existence of spiny issues of detrimental phase transformation at high voltage, poor structural stability, slow ion diffusion kinetics and low working voltage [4,5]. Typically, the promising cathode materials for SIBs mainly include layered sodium transition metal oxides, Prussian blue and its analogs, as well as polyanionic compounds [6,7]. Among them, polyanionic compounds that benefit from the "inductive effect"of polyanion groups have been widely studied because of their high cycle stability and voltage platform [8]. The most typical one is $Na_3V_2(PO_4)_3$ (NVP) with an open 3D NASICON framework enables rapid Na^+ transit. The advantages such as attractive theoretical capacity of 117.6 mAh g^{-1}, high operating voltage of 3.4 V (V^{3+}/V^{4+}) and the good air/thermal stability make NVP cathodes become research hotspot in recent years [9–11]. The critical obstacles that restrict the practical applications of NVP in SIBs are its low intrinsic electrical conductivity and slow

* Corresponding author.
** Correspondence to: Y. Zhao, Shanxi-Zheda Institute of Advanced Materials and Chemical Engineering, Taiyuan 030006, PR China.
E-mail addresses: luhg@sxu.edu.cn (H. Lv), zhaoyun@sxu.edu.cn (Y. Zhao).
[1] The authors contributed equally to this work.

https://doi.org/10.1016/j.est.2025.115378
Received 30 September 2024; Received in revised form 30 December 2024; Accepted 7 January 2025
Available online 15 January 2025

interfacial diffusion kinetics, which inevitably affect the rate capability and cycling stability.

Diverse strategies have been proposed for the modification of NVP, such as nano engineering [12], elemental doping [13] and the combination with carbon materials [14–17]. Especially, the construction of NVP nanostructures associating with the modification of carbon coatings or carbon matrices can prominently enhance the electric conductivity and ion diffusion efficiency of electrode materials. Furthermore, the nanocrystallization of NVP from a bulk can alter the charge storage behavior from battery type to pseudocapacitive type. The increased contact area between the surface of NVP crystals and electrolyte facilitate more surface redox reactions and nonfaradaic storage contribution, resulting in prominently elevated rate performance [18]. Besides nanocrystallization, a recent study demonstrates the amorphization of NVP can also promote the creation of pseudocapacitance. Very different from the sodium intercalation behavior in a well-crystallized NVP structure, the Na^+ diffusion in the loose structure of amorphous NVP is random and even without clear two-phase interface. The weak interactions among the adjacent intercalated sodium ions make the two-phase equilibrium state hard to be achieved, leading to a single-phase electrochemical transition mechanism and a plateau-free charge/discharge process [19,20].

Thermal treatment is an essential step during the fabrication procedure of cathode materials, which produces profound influence on microstructures and electrochemical performance. At present, the common method for synthesizing NVP is to sinter the reaction precursors at high temperature (700–850 °C) in an inert gas atmosphere, so that the pyrolysis and solid phase reactions can be initiated and performed to form well crystallized and structurally stable NVP components [21]. Although this method is widely employed, it is time-consuming and has low efficiency in energy utilization. Moreover, the slow rising/cooling rate and long sintering duration result in the loss of volatile elements and the low yield of carbon components [2]. Therefore, the development of more efficient and energy-frugal means for thermal treatment of cathode materials is of great significance for practical large-scale production and should be highly desired.

As a newly emerged synthetic method, flash Joule heating (FJH) technology is a high-efficient sintering route especially for carbon materials and ceramics, which enables the transformation of raw materials into target products at tunable high temperature within a few seconds or even less than one second. Since Tour's group reported the gram-scale preparation of turbostratic graphene by a FJH technology in 2020 [22], tremendous research enthusiasm has been paid in numerous application fields, such as the ultrafast self-heating synthesis of Mo_2C/MoC/carbon nanotube catalysts for hydrogen evolution reation [23], the construction of $Co_4N/Mo_{16}N_7$ arrays for electrocatalytic hydrazine oxidation [24], the recovery of precious metals from waste [25], and the fabrication of a honeycomb carbon nanofiber/high-entropy alloy composite for electromagnetic wave adsorption [26]. In the research field of electrode materials for rechargeable batteries, several pioneer attempts have been carried out [2,27,28]. Chen's group reported a carbon coated $Na_3V_2(PO_4)_2F_3$ cathode by high-temperature shock strategy within 10 s [28]. Benefited from the carbon hybridized dense structure with high tap density, a high reversible capacity of 103.4 mAh g^{-1} and superb capacity retention of 84.2 % after 1000 cycles were achieved. Wu et al. developed an ultrafast carbothermal shock strategy to synthesize niobium-based oxide anodes with Wadsley-Roth phase structures [27]. The liquid-phase assisted synthesis reactions that were far away from equilibrium facilitated the generation of oxygen vacancies and rich lattice dislocations, resulting in accelerated Li^+ diffusion kinetics and improved fast-charging performance. In view of the favorable effects of these pioneering attempts on developing high-performance electrode materials, more foundational researches should be done to further flourish the application domains of FJH technology in rechargeable batteries.

Herein, we forward to develop NVP cathode materials for SIBs by a designed FJH technology. An ultrafast synthesis of a carbon-modified NVP composite is realized by carbothermal reduction of the precursor mixture at 1000 °C with thermostatic time of 60 s. The short thermal shock time and rapid cooling rate create some beneficial effects in the resulting NVP microstructure, such as the higher conductivity, the remarkably decreased dimension of the NVP particles and the formation of the richer oxygen vacancies than that of the control sample fabricated by a routine thermal treatment. More importantly, the rapid FJH process results in the formation of a special nanocrystal/amorphous phase-mingled NVP structure. These structural features contribute to more pseudocapacitive sodium storage behaviors and accelerated e^-/ion diffusion kinetics, thereby substantially elevating the cycling stability and rate performance. This study further demonstrates the great development potential of FJH technologies for exploiting high-performance cathode materials in rechargeable batteries.

2. Experimental section

2.1. Synthesis of the NVP precursor

All of the chemicals were analytical grade without further purification. Flash graphene was provided by Taiyuan Saiyin New Materials Co., Ltd., which was fabricated through a FJH method at 3200 K with Cabot carbon black (BP2000, USA) as the raw material. The NVP precursor was prepared by a ball-milling method with citric acid and glycine as the co-complexing agent [29]. First, 11.0 mmol of glycine, 2.2 mmol of citric acid, 4 mmol of NH_4VO_3, 6 mmol of $NaNO_3$ and 6 mmol of $NH_4H_2PO_4$ were added into 10 mL deionized water and continuously stirred for 30 min to form a solution. Meanwhile, 50 mg of flash graphene was dispersed in 10 mL ethanol to form a suspension. By mixing the solution and the suspension, the mixture was ball-milled at 300 r min^{-1} for 6 h. Finally, the dispersed suspension was baked in a vacuum oven at 80 °C for 12 h to obtain the NVP precursor.

2.2. Synthesis of the NVP/C composites by a FJH technology

The employed FJH reaction system was in the same to that of previous work [30,31], where the photograph of the key reaction chamber was displayed in Fig. S1. Briefly, 150 mg of the ground precursor was placed in a quartz tube (inner diameter = 8 mm, length = 70 mm) with conductive graphite plugs at the two end of the quartz tube to build a relatively enclosed space. The inner wall of the quartz tube was covered by a carbon paper with a thickness of ~50 μm. The quartz tube was fixed at the reaction frame, and the knob was rotated to squeeze the samples for reaching a proper resistance of <5 Ω. Subsequently, a vacuum environment was imposed for the convenience of gas release and the prevention of materials from oxidation during the FJH reaction process. Under an alternating current mode, the rated condition of a voltage of 36 V and a current of 83 A was modulated to generate a stable power supply. Through program setting, the sintering reactions that varied the heating temperature from 800 to 1200 °C and varied the thermostatic time from 30 to 90 s were carried out. Specially, the obtained sample that fabricated at 1000 °C for 60 s was denoted as F-NVP/C-1000.

2.3. Synthesis of the NVP/C composite by a routing annealing method

The annealing process of the NVP/C precursor was performed in a routing tube furnace abide by the optimized temperature program which has been established in our previous work [29]. At a rising rate of 5 °C min^{-1}, the ground NVP precursor was preheated at 350 °C for 3 h and annealed at 800 °C for 5 h in an Ar atmosphere. After naturally cooling down, the product was obtained, which was named as R-NVP/C-800.

2.4. Material characterizations

X-ray diffraction (XRD, Bruker D8, Germany) tests were performed using Cu-Kα (λ = 1.54056 Å) radiation to characterize the phase composition and crystal structures. The morphologies and texture of the NVP composites were observed via a scanning electron microscopy (SEM JIOL, JSM-7001F) and a transmission electron microscopy (TEM, FEI-G2-F30). The elemental composition was detected by energy dispersing spectroscopy (EDS). The Fourier transform infrared (FTIR) spectra were measured by a Bruker Tensor 27 instrument within 500–2500 cm^{-1}. The carbon content in the samples was estimated by thermogravimetric analysis (Netzsch STA 449F3) under an air atmosphere (heating rate: 10 °C min^{-1}). The Raman spectrogram (HORIBA JY LabRAM HR Evolution) was carried out to analyze the carbon components with an excitation laser beam wavelength of 532 nm. X-ray photoelectron spectroscopy (XPS, Thermo Fisher Scientific K-Alpha) was employed to identify the valence states of elements on surface. The N_2 adsorption/desorption behaviors were analyzed on a BET surface analyzer (Quantachrome Autosorb-iQ3-MP/Kr). The electron paramagnetic resonance (EPR) tests were operated on Bruker E500.

2.5. Electrochemical measurements

The coin-type half-cells (CR2025) were assembled in an argon-filled glove box (O_2 and H_2O were below 0.1 ppm) with a Na metal foil as the counter electrode. 1 M $NaClO_4$ dissolved in dimethyl carbonate/ethylene carbonate/ethyl methyl carbonate (v:v:v = 1:1:1) with 2 % fluoroethylene carbonate was applied as the electrolyte. The active material, flashing graphene and polyvinylidene fluoride were mixed at a mass ratio of 8:1:1 with *N*-methyl-2-pyrrolidone as the solvent. After coating on an Al foil, the uniform mixture was dried at 120 °C for 12 h in a vacuum oven. The foil was punched into discs with a diameter of 12 mm, and the average loading density of active components was 1.6–1.8 mg cm^{-2}. The galvanostatic charge-discharge (GCD) was implemented on a battery testing system (LAND CT 2001 A) within a voltage window of 2.2–4.0 V (vs. Na^+/Na). Cyclic voltammetry (CV) and electrochemical impedance spectroscopy (EIS) tests (frequency range: 0.01 Hz to 100 kHz) were conducted on an electrochemical workstation (CHI660E, Chenhua). The full cell was assembled by coupling the F-NVP/C-1000 and a pre-sodiated commercial hard carbon (YHC-1, BAISIGE Co., Ltd.) as the cathode and anode materials, respectively. The pre-sodiation process of hard carbon is based on the previously reported method [32]. The N/P (Negative/Positive) ratio was fixed at approximate 1.05.

2.6. The COMSOL simulation of the FJH process

The electric heating furnace was consisted of three parts: stainless steel electrodes, high conductivity carbon paper, and the NVP/C sample wrapped in a carbon paper. The structure of the Joule heating furnace was schematically described in Fig. S2. In order to reduce the amount of calculation, only 1/4 of the heating furnace was simulated. Table S1 listed the main properties (electrical conductivity σ, thermal conductivity *k*, density ρ, and heat capacity C_p) of the specific materials. The Joule heating involved two processes: current conservation and thermal conservation. The conservation equation and initial and boundary conditions were as follows [33]:

$$\rho C_p \frac{\partial T}{\partial t} = \nabla \bullet (k \nabla T) + Q_e$$

$$\frac{\partial(\nabla \bullet \nabla V)}{\partial t} = \nabla \bullet (-\sigma \nabla V)$$

The initial boundary conditions:

$$t = 0, T = 293.15\ K, V = 0\ V.$$

The boundary conditions:

$$z = 0, q = h(T_{external} - T), V = V0.$$

$$z = z, q = h(T_{external} - T), V = 0$$

All other boundaries for the electric current conservation equation were electric insulation. While for the heat transfer, radiation heat dissipation was considered, and heat loss by radiation was formulated as follows:

$$q = \varepsilon \sigma_{radiation} \left(T_{external}^4 - T^4\right)$$

in which, ε is the surface emissivity and $\sigma_{radiation}$ is Stefan-Boltzmann constant.

3. Results and discussion

3.1. The FJH process analysis for the preparation of F-NVP/C composites

As depicted in Fig. 1a, the facile FJH method is utilized to realize the ultrafast synthesis of the F-NVP/C composites by sintering the mixed NVP precursor. In contrast to the time-consuming annealing program operating in a traditional tube furnace (Fig. 1b), the rising/cooling rates and duration time of the temperature in a FJH process are exponentially discrepant. Typically, by monitoring from the real-time temperature curve (Fig. 1c), the rising and cooling rates for the sintering of F-NVP/C-1000 are estimated to be 37.6 and 16.6 °C s^{-1}, respectively. The time-dependent voltage and current profiles (Fig. 1d) are concordant in tendency, demonstrating a progressive high power for the rapid creation of Joule heat. To further understand the thermal field distribution during the FJH process, a COMSOL finite element analysis is carried out. Fig. S3a shows the voltage-time diagram used for simulation. The voltage rises from 0 to 12 V within 30 s, and then drops to 8 V within 20 s. After maintaining the voltage of 8 V for 50 s, the voltage drops to 0 V. From Fig. S3b, it can be seen that the center temperature of the quartz tube rapidly increases to 1150 °C as the voltage rises. During the voltage drop and holding stage, the center temperature slightly decreases. Subsequently, when the voltage goes down to 0, the temperature drops rapidly due to the factors such as radiation and heat dissipation. Fig. 1e displays the temperature maps of the central section (upper) and cross-section of the heating furnace at different time (lower). In the early stage of heating, conductive carbon paper generates a large amount of heat and heats the NVP sample wrapped in it through thermal conduction. The temperature difference between the center and outer wall is about 30 °C (10 s). As the heating proceeds, the temperature of the sample gradually increases, and the temperature gradient between the center and outer wall of the sample also gradually increases to 90 °C (30 s). Afterwards, due to the decrease in voltage, the internal temperature gradient decreases, and the overall temperature tends to be uniform, which is beneficial for the consistency of material preparation. After stopping heating, the center temperature will be higher than that of the outer wall due to heat dissipation. The above simulation results indicate that voltage is the decisive factor affecting the temperature distribution in the NVP sample. Adjusting the voltage appropriately is important to reduce the temperature gradient of the bed and realize good material uniformity. During the preparation process of the NVP precursor by ball milling, 5 wt% flash graphene with high electric conductivity is introduced to fulfill the resistance requirement for initiating the discharge of the equipped capacitor bank. Moreover, the dispersive flash graphene is helpful to diminish thermal resistance between precursor particles and improve the component uniformity of the obtained NVP products. The SEM and HRTEM images of flash graphene are shown in Fig. S4, where the sphere-like morphology and twisted few-layer graphene structure with high crystallinity are presented.

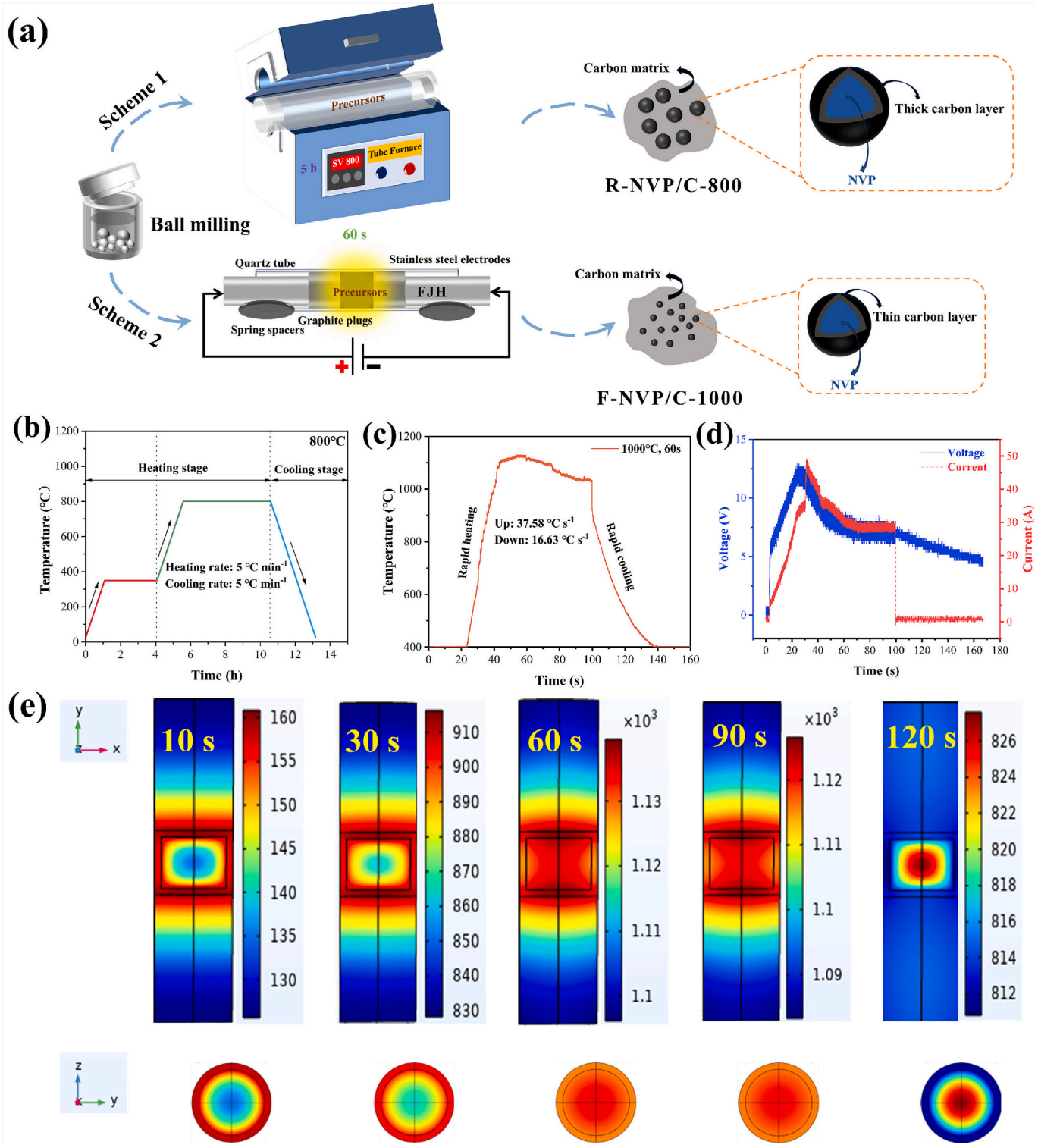

Fig. 1. (a) Schematic illustration of the two synthesis routes for NVP/C. (b) The temperature-time curve for the preparation of R-NVP/C-800. (c) The temperature-time curve for the preparation of F-NVP/C-1000. (d) The real-time voltage and current curves. (e) The thermal field distribution maps at different simulation time (upper: Section along the center of the heating furnace; lower: Cross section of the heating furnace center).

3.2. Microstructure investigation of the F-NVP/C composites

To explore the optimized parameters for the fabrication of the F-NVP/C composites, the condition experiments that vary the anneal temperature and duration time are carried out. The two factors are demonstrated to have profound influence on the microstructure and electrochemical performance of the obtained NVP composites. Fig. S5a displays the XRD patterns of the F-NVP/C composites prepared at different sintering temperature of 800, 1000 and 1200 °C. All of the three composites exhibit a rhombohedral NVP phase (JCPDS#97–024-8140) with the space group of $R\bar{3}c$ [34], suggesting the successful synthesis of NVP materials by the FJH method. The crystallinity of the obtained NVP has obvious distinction. With the elevation of sintering temperature, the intensity of the diffraction peaks gradually increases.

The phenomenon would be attributed to the accelerated solid-phase reaction dynamics at higher temperature. However, when the sintering temperature reaches 1200 °C, evident diffraction signals assigning to a divalent vanadium oxide (JCPDS#97–002-8681) are detected. The improper high temperature results in the excessive reduction of vanadium species and the formation of low-valent impurities by carbothermic effect. The XRD patterns of the F-NVP/C composites fabricated at different thermostatic time are shown in Fig. S5b. It is found the crystallinity of NVP is less sensitive to duration time, while the excessive sintering (90 s) leads to the distinct increase of the impurity content of VO. The too poor crystallinity of NVP and the existence of the VO impurity are detrimental to electrochemical performance. As demonstrated in Fig. S6 and Fig. S7, the low crystallinity arising from the insufficient sintering (low reaction temperature of 800 °C or short thermostatic time of 30 s) result in inferior specific capacity and cycling stability. On the other hand, the rate performance is deteriorated due the inopportunely increased crystallinity and the production of noticeable impurity, especially in the case with a high sintering temperature of 1200 °C.

On the bases of the optimization above, systematical microstructure investigation and electrochemical behavior analyses of F-NVP/C-1000 are carried out hereafter. Fig. 2a compares the XRD patterns of F-NVP/C-1000 and R-NVP/C-800. All of the diffraction peaks in F-NVP/C-800 also can be indexed to the rhombohedral NVP (JCPDS#97–024-8140) with high purity, indicating that the FJH process does not cause the phase structure change of NVP. However, the drastically shortened thermostatic time and rapid cooling rate during the FJH process give rise to the lower and broader peak signals of F-NVP/C-1000. The weaker diffraction signals could be due to the smaller crystallite size and particle dimension of NVP [35]. From the estimated average crystalline size (L_c) by Scherrer formula (Table S2), it is found the value of L_c for F-NVP/C-1000 (43.6 nm) is smaller than that (58.7 nm) for R-NVP/C-800. The crystal structure information of NVP is further determined by Rietveld refinement with the General Structure Analysis System II (GSAS-II) program, and the fitted profiles are shown in Fig. 2b and Fig. S8. From the calculated crystallographic data (Table S3), the lattice parameters of F-NVP/C-1000 are slightly larger than the corresponding values of R-NVP/C-800. The enlarged crystal cell volume is beneficial for improving the structural stability of NVP and facilitating Na^+ diffusion during sodiation/desodiation [36]. Moreover, the specific atomic occupations of R-NVP/C-800 and F-NVP/C-1000 are displayed in Tables S4-S5 with

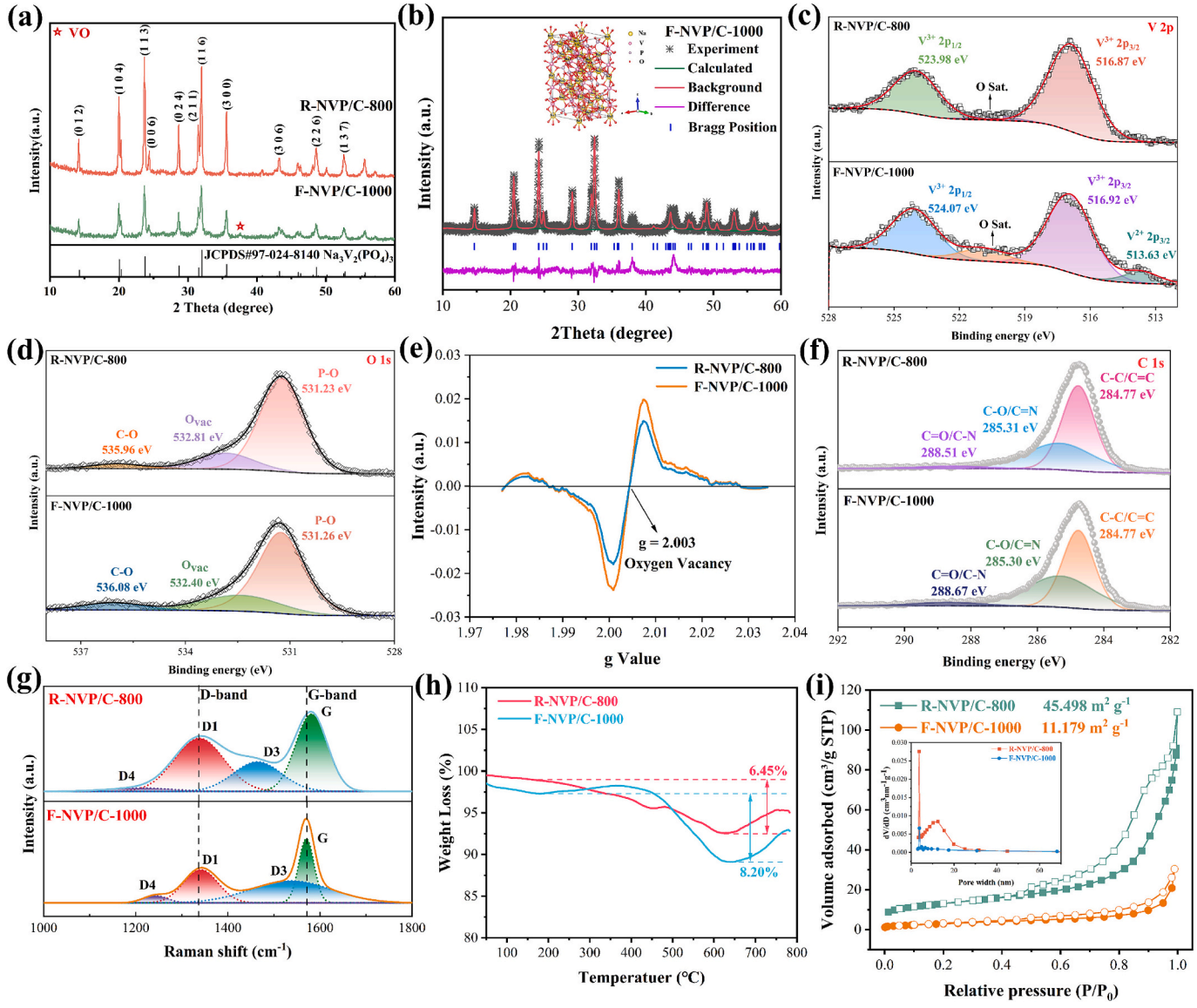

Fig. 2. (a) Representative XRD patterns of R-NVP/C-800 and F-NVP/C-1000. (b) The Rietveld-refined XRD profile of F-NVP/C-1000. The high-resolution XPS spectra of V 2p (c), O 1 s (d) and C 1 s (f) for R-NVP/C-800 and F-NVP/C-1000, respectively. (e) The g-factor profiles; (g) The Raman spectra; (h) The TGA curves; (i) The nitrogen adsorption-desorption isotherms with the corresponding pore size distribution of R-NVP/C-800 and F-NVP/C-1000.

favorable reliability according to the high fit degree.

The surface element composition and bonding states are determined by XPS. The survey spectra (Fig. S9) disclose that both of F-NVP/C-1000 and R-NVP/C-800 are mainly composed of V, P, Na, O, N and C elements. The decipherable signals of N are rooted from the pyrolysis residual of glycine during the sintering process, where the graphitic N components in N-doping are beneficial to improve the electric conductivity of carbon products [29,37]. The element content of N in F-NVP/C-1000 calculating through integral area is 1.91 times of that in R-NVP/C-800 (Fig. S10), suggesting less nitrogen loss during the FJH preparation process due to the very short annealing time. The deconvoluted V 2p spectra are shown in Fig. 2c, in which the peaks at 524.0/524.1 eV and 516.9/517.0 eV are assigned to V^{3+} $2p_{1/2}$ and V^{3+} $2p_{3/2}$, respectively [35]. It is noticed that an additional peak corresponding to V^{2+} $2p_{3/2}$ is detected at a lower binding energy of 513.6 eV for F-NVP/C-1000 [38]. The result further confirms the existence of VO, which is consistent with the XRD observation. After fitting, the content of VO in the vanadium-involved species is estimated to be 1.54 %. The high-resolution O 1 s spectra (Fig. 2d) provide more information for the NVP crystal structures. Besides the characteristic peaks of C—O and P—O bonds at 536.1/536.0 eV and 531.2/531.1 eV, the broad peak located at 532.4 and 532.8 eV attributing to oxygen vacancies also can be observed for F-NVP/C-1000 and R-NVP/C-800, respectively [8,39]. The atomic content of oxygen vacancies in F-NVP/C-1000 calculating through integral area is 1.35 folds to that of R-NVP/C-800, suggesting more abundant oxygen vacancies exist in the former. To further prove the existence of oxygen vacancies in the two NVP/C composites, EPR tests are conducted. Fig. S11 shows the original EPR curves of the two samples. After a fitting, the g-factor maps are depicted. As shown in Fig. 2e, both of them have a conspicuous resonance signal at $g = 2.002$, verifying the existence of oxygen vacancies in the NVP lattices [40,41]. Moreover, the resonance intensity ratio between F-NVP/C-1000 and R-NVP/C-800 is 1.43, which is in line with the XPS analyses. It is noted that some oxygen vacancies are also formed in R-NVP/C-800. This may be because the oxygen atoms in NVP crystals dissociate from their original positions and combine with the N atoms in carbon layer during high temperature treatment [41]. The higher oxygen vacancy content in F-NVP/C-1000 is caused by the ultrafast solid-phase reaction process away from equilibrium. The substantially accelerated reaction rate results in increased point defects and lattice dislocation in NVP crystals [27]. These defects can promote Na^+ diffusion by lowering migration energy barrier and reducing the interaction between Na^+ and V-O/P-O frameworks. Furthermore, the abundant oxygen vacancies can narrow the band gap and improve the conductivity of NVP [42]. The bonding state of carbon is revealed by high-resolution C 1 s spectra. As shown in Fig. 2f, the C=C/C-C bonds are located at the position of 284.8 eV, and the Lorenz peaks sited at around 288.7 eV and 285.3 eV can be classified as C=O/C-N and C-O/C=N, respectively [43,44]. The carbon surface functional characteristics of F-NVP/C-1000 and R-NVP/C-800 are similar, indicating the analogous pyrolysis behavior of organic components during the FJH process to that of routine annealing. The nature of carbon components in the two NVP/C composites are further analyzed by Raman spectra (Fig. 2g). According to the Lorentzian function [45], the spectra within the Raman shift of 1100–1800 cm^{-1} can be deconvoluted into four subpeaks. The area ratio between the D1 peak at 1338 cm^{-1} and the G peak at 1584 cm^{-1} (A_{D1}/A_G) is related to the defect degree of carbon materials [46]. The A_{D1}/A_G value (1.07) of F-NVP/C-1000 is smaller than that (1.16) of R-NVP/C-800, suggesting a more ordered carbon structure with less defects and higher conductivity is formed after suffering the FJH treatment. The result suggests that the crystallization behaviors of the carbon component and the NVP component are very different during the FJH process, which would be ascribed to the sintering kinetics difference of the two components since carbon has much high thermal conductivity than NVP.

The carbon contents in the two NVP samples are determined by TGA. From the thermogravimetric curves (Fig. 2h), the mass loss below 150 °C is attributed to the removal of absorbed water. Subsequently, the weight continuously decreases due to the consumption of carbon by oxygen. During this stage, the oxidation reactions of carbon in F-NVP/C-1000 are more sluggish than that in R-NVP/C-800, reflecting the lower reactivity probably resulting from the higher crystallinity and the existence of the fewer defects in carbon framework by FJH. After rising to 650 °C above, an obvious weight increase is observed. And this phenomenon is ascribed to the oxidation of V^{3+} to V^{4+} and V^{5+} [47]. Based on the thermal loss behaviors, the carbon contents in F-NVP/C-1000 and R-NVP/C-800 are approximate 8.20 wt% and 6.45 wt%, respectively. The result indicates that the FJH process with short annealing time effectively avoids the carbon loss upon high temperature, which is in accordance with the previous literatures [2].

The morphologies and microstructures of the samples are visualized by SEM and TEM observations. It is seen from Fig. 3a, b and Fig. S12 that both of the two NVP/C composites present a hybrid structure where NVP particles are anchored on a carbon matrix. The size of the NVP particles in R-NVP/C-800 is much larger than that in F-NVP/C-1000, and the dispersity in the carbon matrix is poor. Moreover, obvious sintering phenomenon between the adjacent NVP particles is discovered, which would be caused by the tedious treatment under high temperature. In contrast, the NVP particles in F-NVP/C-1000 manifest relatively uniform size and a homogenous dispersion, demonstrating the transitory thermal shock and quick cooling rate effectively suppress the crystal growth and mutual fusion of the nascent NVP nanoparticles. The TEM images also reveal the structural difference of the two samples. As shown in Fig. 3c and d, the dimension of a single NVP particle in F-NVP/C-1000 is more intuitively proved to be much smaller. These NVP nanoparticles are firmly associated with the carbon matrix, constructing a robust hybrid structure. The HRTEM observation is further conducted to analyze the fine structure of the composites. In the typical HRTEM image (Fig. 3e) of R-NVP/C-800, a well-grown NVP crystal can be distinguished. The clear lattice fringe with an interplanar distance of 0.37 nm is corresponded to (113) plane of NVP. In addition, a thick and amorphous carbon coating of around 12.5 nm is covered on the NVP particles. Although the thick carbon coating can buffer volume expansion and improve conductivity of NVP, the Na^+ transformation will be constrained, leading to slow diffusion kinetics [41]. As a sharp comparison, the HRTEM image (Fig. 3f) of F-NVP/C-1000 reveals much smaller crystal particles. The crystallinity is relatively poor to that in R-NVP/C-800, demonstrating the quite different texture feature of NVP synthesized by the FJH route. Moreover, some amorphous NVP phases which are mingled with ultrasmall NVP nanocrystals of <5 nm also can be observed (Fig. S13a), indicating the very short annealing time and rapid cooling prominently restrain the nucleation and growth of the as-formed NVP components. The existence of amorphous NVP phase can be further verified by FTIR spectra (Fig. S14). Notably, despite similar V—O peaks around 631 cm^{-1} in both samples, F-NVP/C-1000 exhibits lower P—O stretching bands compared to those in R-NVP/C-800, indicating weaker chemical bonds and a more fragile framework in F-NVP/C-1000. Compared to crystals, amorphous materials will interfere the vibration frequency of chemical bonds with a slight shift due to the disordered structure of atoms [48]. Therefore, the left shift of P—O band in F-NVP/C-1000 further confirms the existence of amorphous phase. The proportion of amorphous NVP phase in F-NVP/C-1000 is calculated by X-ray diffraction method [49], accounting for 78 %. It is also found that the carbon layer covered on NVP is only ~2.3 nm (Fig. S13b). The difference in carbon coating thickness would impose some influence on rate capability of the two NVP samples. In addition, the selected area electron diffraction patterns of both samples present typical characteristic of NVP structures. The pattern for F-NVP/C-1000 is more indistinct, which is in line with the lower crystallinity of NVP as is observed in HRTEM images. One also should be noticed that some flash graphene fragements are mingled with the NVP nanoparticles, and the tight contact between the two components are observed due to the ball-milling effect and the subsequent thermal shock. The modification of flash graphene on the surface of

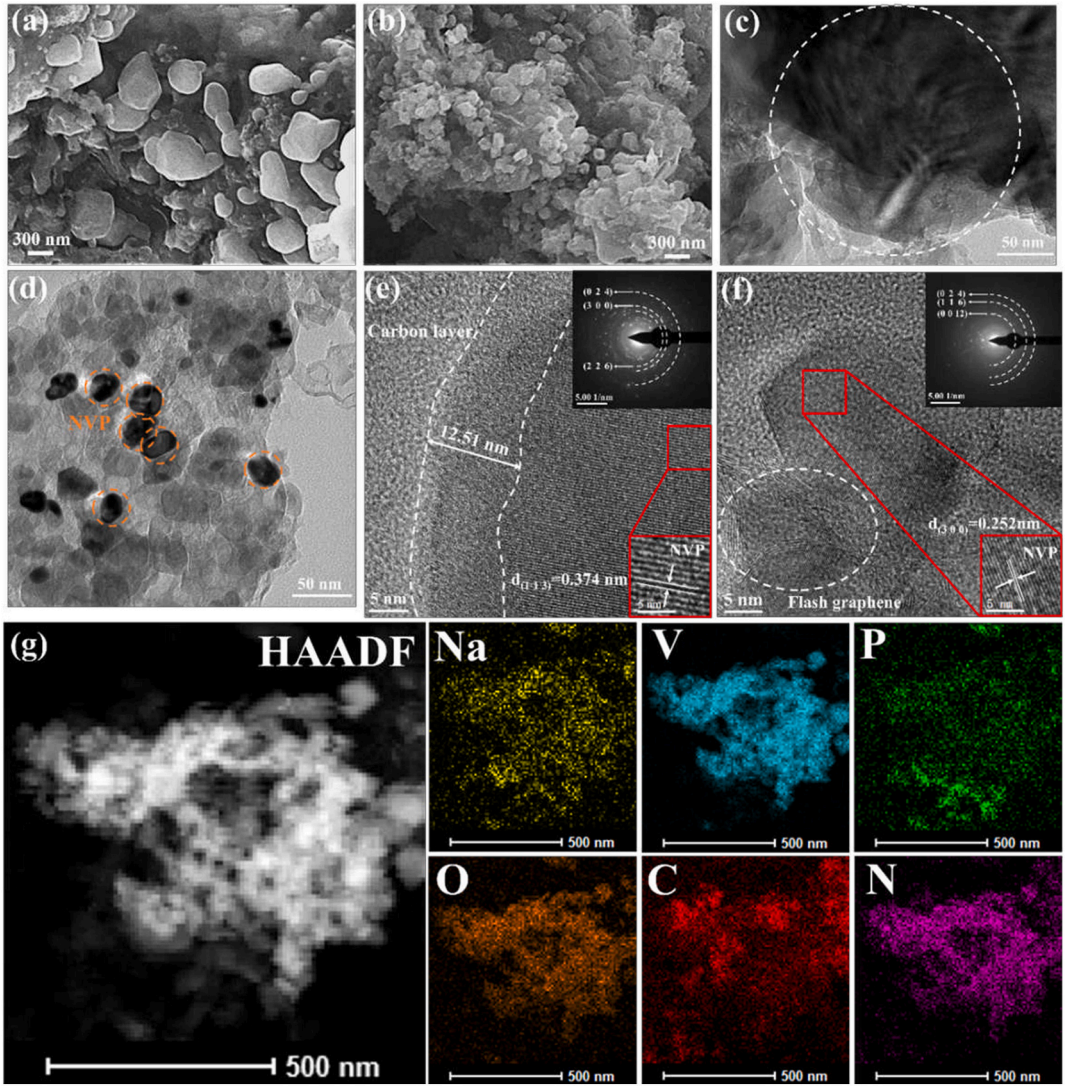

Fig. 3. (a) and (b) SEM images of R-NVP/C-800 and F-NVP/C-1000, respectively. (c) and (d) TEM images of R-NVP/C-800 and F-NVP/C-1000, respectively. (e) and (f) HRTEM images of R-NVP/C-800 and F-NVP/C-1000, respectively. The insets are the corresponding selected area electron diffraction (SAED) patterns. (g) The high-angle annular dark-field profile of F-NVP/C-1000 and EDS element mapping.

NVPs further improves the conductivity and contributes to faster charge transfer. As declared in Chen's group [28], the high-temperature shock is apt to form a denser material structure accompanying the rapid crystallization of precursors, resulting in reduced specific surface area. The statement is in agreement with our present study to some degree. From the nitrogen adsorption/desorption isotherms (Fig. 2i), the Brunauer-Emmett-Teller specific surface area of R-NVP/C-800 and F-NVP/C-1000 is calculated to be 45.5 and 11.2 $m^2\ g^{-1}$ respectively, demonstrating the FJH process makes for a denser hybrid structure and substantial decrease of specific surface. Correspondingly, the pore size distribution curves basing on the Barrett-Joyner-Halenda model are displayed in the inset of Fig. 2i. The pore concentration at 17.6 nm in R-NVP/C-800 is ascribed to the aggregation of large NVP particles [28]. Very differently, these larger pores vanish away and the average pore size shifts to 3.8 nm in F-NVP/C-1000. This behavior reflects the much improved dispersity and diminished dimension of NVP particles, which well attests to the SEM and TEM observation. The component uniformity of F-NVP/C-1000 is examined by EDS elemental mapping. As shown in Fig. 3g, the even distribution of Na, V, P, O, C and N elements well depicts a homogenous NVP/nitrogen-doped carbon matrix configuration.

3.3. Electrochemical behavior comparison of the F-NVP/C-1000 and R-NVP/C-800 electrodes

The electrochemical behaviors of the R-NVP/C-800 and F-NVP/C-1000 electrodes are investigated by assembling coin-type half-cells with sodium foils as the counter/reference electrodes. Fig. 4a shows the cyclic voltammetry (CV) curves of the two electrodes at a scan rate of 0.1 mV s^{-1}. The predominant cathodic and anodic peaks at around 3.4 V is corresponding to the reversible V^{3+}/V^{4+} state transition [50]. The cleavage in the cathodic peak, which is commonly observed in NVP materials, is ascribed to the two-step migration behavior of Na^+ during sodiation [51]. The more serious cleavage of the cathodic peak and the larger polarization voltage difference (0.230 V) between the anodic and cathodic peaks of the R-NVP/C-800 electrode signify the more sluggish electrochemical reaction kinetics. In contrast, the F-NVP/C-1000 electrode has a decreased polarization voltage difference of 0.182 V and more sharp redox peak profiles, manifesting a very positive effect of the FJH route for improving electrochemical reaction reversibility and sodium storage kinetics in NVP structures.

The CV curves (Fig. 4b and Fig. 4d) at different sweep speeds from 0.2 to 1.0 mV s^{-1} are conducted to further evaluate the sodium storage behaviors. For both of the electrodes, the anodic and cathodic peaks shift

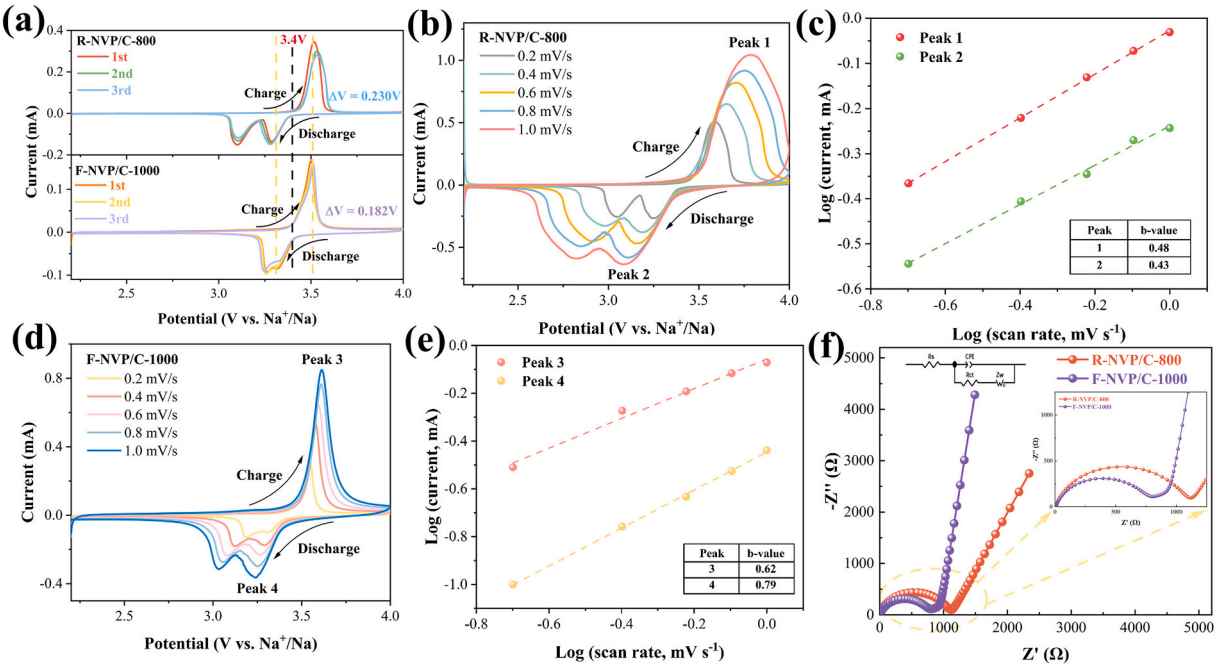

Fig. 4. (a) Typical CV curves for the first three cycles of the R-NVP/C-800 and F-NVP/C-1000 electrodes at a scan rate of 0.1 mV s^{-1}. (b) and (d) The CV curves of the R-NVP/C-800 and F-NVP/C-1000 electrodes at different scan rates, respectively. (c) and (f) The log I_p vs log v curves and the Nyquist plots of the R-NVP/C-800 and F-NVP/C-1000 electrodes, respectively.

to right and left respectively with increasing scan rate due to polarization [51]. Different from the quite broadened peak profiles of the R-NVP/C-800 electrode at higher scan rates, the sharp redox peaks of the F-NVP/C-1000 electrode are still maintained even at the high sweep speed of 1.0 mV s^{-1}, reflecting much improved polarization. Fig. 4c and Fig. 4e illustrate the log (*ip*) versus log (*v*) plots of the redox peaks for the two electrodes. The relationship between the peak current (*ip*) and the square root of corresponding sweep rate (*v*) is quantitatively described by the equation: $log(i) = blog(v) + loga$ [52]. The value of *b* is an indicator of the charge storage mechanism. That is, values close to 0.5 suggest the characteristic of diffusion-dominated processes, while those approaching to 1 mean the charge storage is dominated by surface pseudocapacitive behaviors [52]. For the R-NVP/C-800 electrode, the *b*-values of the oxidation and reduction peaks are 0.48 and 0.43 respectively, which indicates that the sodiation/desodiation reactions are mainly controlled by Na^+ diffusion within the NVP host. Differently, the higher *b*-values of 0.62 and 0.79 for the oxidation and reduction peaks of the F-NVP/C-1000 electrode signify more pseudocapacitive behaviors during the electrochemical redox process. Fig. S15 shows the quantitative results of separate capacitive and diffusion-controlled contribution at different scan rates. The pseudocapacitance contribution ratios of the two electrodes increase with the rising scan rates. The value of F-NVP/C-1000 is up to 91 % at 1.0 mV s^{-1}, which is much higher than that of R-NVP/C-800. The much increased capacitive charge storage behaviors would be attributed to the nanocrystallization of NVP particles and the existence of amorphous NVP components, as has been demonstrated in Ma's work [53]. The more pseudocapacitive sodium storage is responsible to decreased electrochemical polarization, facilitating enhanced rate capability.

The EIS measurements can further illustrate the reasons for the improved polarization of F-NVP/C-1000. The Nyquist plots (Fig. 4f) for both of the R-NVP/C-800 and F-NVP/C-1000 electrodes are consisted of a semicircle in the high-intermediate-frequency region relating to charge transfer resistance (R_{ct}), and a sloping line in the low-frequency region in connection with Warburg impedance (Z_ω) [54]. As shown in Table S6, the R_{ct} value of 785.9 Ω for the F-NVP/C-1000 electrode is smaller than that (1093.0 Ω) of the R-NVP/C-800 electrode, demonstrating the faster charge transfer in the bulk of F-NVP/C-1000. The R_{ct} values are very relevant to electrical resistance of electrode materials. Measured by a four-probe resistivity meter, F-NVP/C-1000 shows an electrical resistivity of 3.97 kΩ cm, which is much lower than that (9.82 kΩ cm) of R-NVP/C-800 (Fig. S16). Moreover, the inclined line in the low frequency region can be applied to calculate the Na^+ diffusion coefficient (D_{Na^+}) by means of the equation: $D_{Na^+} = \frac{R^2T^2}{2A^2n^4F^4C^2\sigma^2}$ [52]. The relationship between Z' and $\omega^{-1/2}$ ($Z' = R_\Omega + R_s + \sigma\omega^{-1/2}$) used for the calculations is displayed in Fig. S17. The calculated D_{Na^+} (Table S6) of the F-NVP/C-1000 electrode is 1.17×10^{-9} cm^2 s^{-1}, which is an order of magnitude higher than that of the R-NVP/C-800 electrode (2.05×10^{-10} cm^2 s^{-1}). The results reflect that the enhanced charge transfer and Na^+ diffusion kinetics contribute to the much alleviated polarization of the F-NVP/C-1000 electrode, which will result in elevated electrochemical performance.

Fig. 5a and b depict the galvanostatic charge/discharge curves of the F-NVP/C-1000 and R-NVP/C-800 electrodes, respectively. The charge and discharge curves of the R-NVP/C-800 electrode present a long voltage plateau at around 3.4 V, according with the typical characteristic of NVP materials with well-developed crystal structures [53]. Very differently, the corresponding characteristic plateau is obviously shortened for the F-NVP/C-1000 electrode. The profound slope-line profiles contribute to more capacitive contribution for sodium storage. The special phenomenon would be ascribed to disorder-induced pseudocapacitive behaviors in amorphous NVP materials [20]. The random and uniform Na^+ diffusion in amorphous NVP structures eliminates the phase equilibrium state between $Na_3V_2(PO_4)_3$ and $NaV_2(PO_4)_3$ during sodium insertion and extraction, resulting in a single-phase reaction-dominated electrochemical process. The Na^+ diffusion modes in NVP hosts can be judged by the interaction parameter between the adjacent ions (*J*). Based on the lattice-gas model and the related formula: $E = E^0 - \frac{RT}{F}ln\left(\frac{x}{1-x}\right) + J(x-0.5)$ [53], the discharge curves of the electrodes are fitted. In F-NVP/C-1000 where nanocrystals and amorphous structures coexist, the law of long-range order is broken, and the interaction between inserted sodium ions is weakened, corresponding to a *J* value of

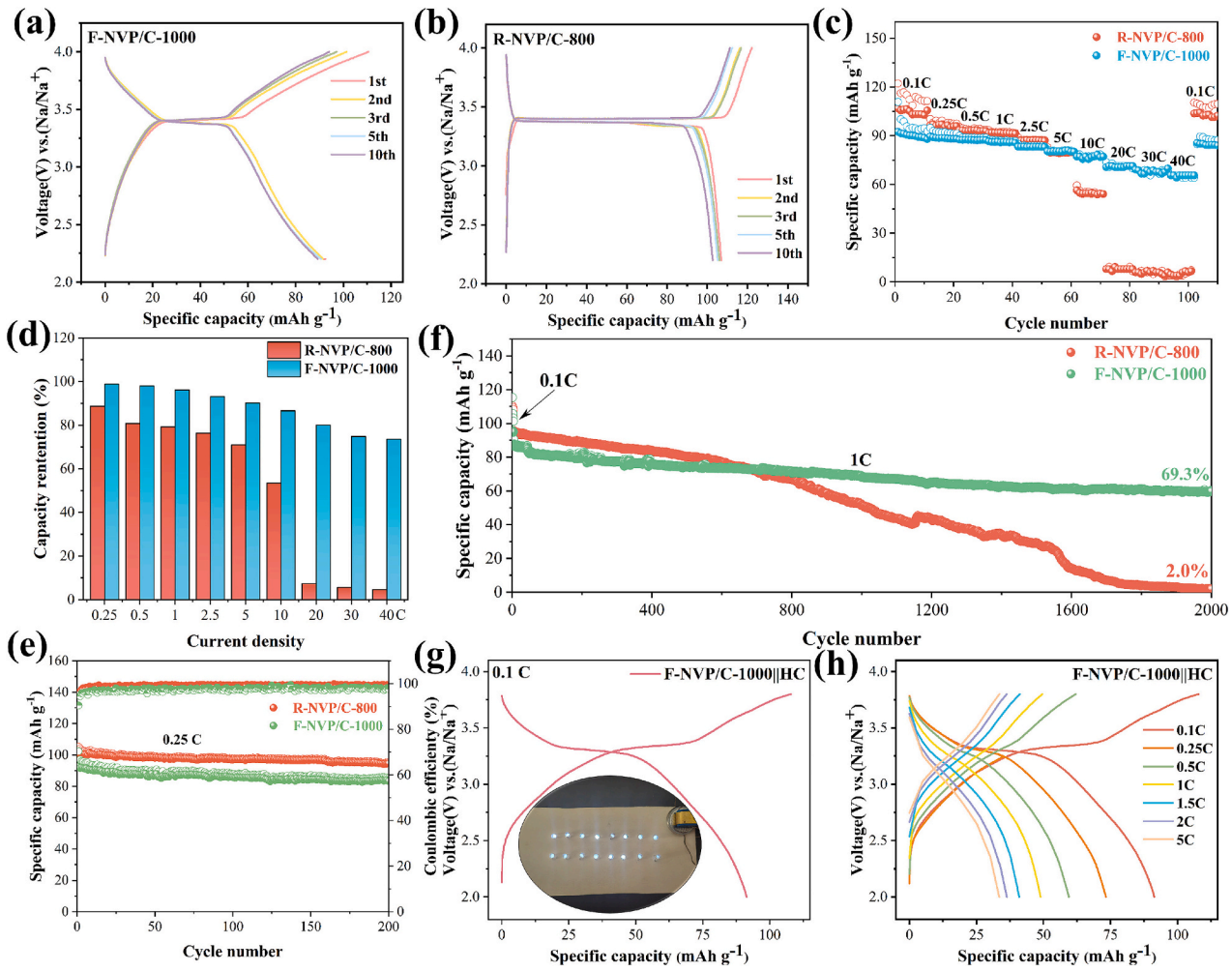

Fig. 5. (a) and (b) The galvanostatic charge/discharge curves at 0.1C. (c) Rate capacity. (d) Capacity retention comparison at different rates. (e) Cycling performance at 0.25C and (f) Long-term cycling stability at 1C. (g) and (h) The charge/discharge curves at 0.1C and at different rates of F-NVP/C-1000||HC full cell, respectively.

<0 and the trend of a single-phase reaction process (Fig. S18a). In contrary, the R-NVP/C-800 electrode presents a higher *J* value of >4RT/F (Fig. S18b). It means that there is a strong repulsive force between the inserted adjacent sodium ions, which makes Na^+ insertion process a local ordered diffusion. To this regard, the *E*-x curve appears a maximum value and a minimum value, and the intercalation and delamination processes manifest a typical two-phase reaction process [20]. The F-NVP/C-1000 electrode releases charge and discharge capacities of 108.9 and 92.5 mAh g^{-1} respectively, reaping an initial Coulombic efficiency (ICE) of 84.9 %. The corresponding capacity values for the R-NVP/C-800 electrode are 119.7 and 105.9 mAh g^{-1} respectively, and the ICE is 88.5 %. The lower charge/discharge specific capacities and ICE of the F-NVP/C-1000 electrode could be attributed to the existence of the VO impurity and the richer surface defects that especially come from the amorphous NVP components. In spite of the slightly lower reversible capacity, the F-NVP/C-1000 electrode exhibits a substantially improved rate capability (Fig. 5c). With the current densities stepwise increasing from 0.1 to 0.25, 0.5, 1.0, 2.5, 5, 10, 20 and 30C, the F-NVP/C-1000 electrode delivers reversible capacities of 92.5, 89.7, 87.6, 86.6, 83.3, 80.4, 77.2, 70.7 and 69.2 mAh g^{-1}, respectively. Remarkably, a high capacity of 65.6 mAh g^{-1} still can be maintained at the ultrahigh current density of 40C, suggesting the rapid capacity response to high charge/discharge rates. The inclusion of amorphous phases significantly increases the proportion of Na2 sites and facilitates reversible deintercalation, contributing to the Na^+ diffusion kinetics and internal stress mitigation during sodium insertion and extraction [48]. In sharp contrast, the rate performance of the R-NVP/C-800 electrode is much inferior especially at the current densities higher than 5C. The disparity between the rate performances of the two electrodes is more intuitively reflected by rate capacity retentions at different current densities (Fig. 5d). Typically, a high capacity retention ratio of 73.6 % is retained at 40C for the F-NVP/C-1000 electrode, while the corresponding value for the R-NVP/C-800 electrode is only 4.6 %. The prominently improved rate performance would be attributed to the accelerated charge transfer and ion diffusion rate of the F-NVP/C-1000 electrode as that have been demonstrated by kinetics analyses above. It is convinced that the diminished particle dimension of NVP, the increased oxygen vacancy concentration and the enhanced electrical conductivity by flash graphene association together contribute to the high rate performance. In addition, the thinner carbon coating on the NVP particles and the featured crystallization characteristic that presents a coexistence of tiny nanocrystals and amorphous NVP components also create a positive contribution.

The cycling performances of the two electrodes are displayed in Fig. 5e. Both of the electrodes show good cycling stability at a low current density of 0.25C. The F-NVP/C-1000 electrode keeps a high capacity retention of 90.6 % after 200 discharge/charge cycles, which is comparable to the value of the NVP/C-800 electrode (91.4 %). To further compare the cycling ability of the electrodes, the long-term cycling tests at 1C are carried out. As shown in Fig. 5f, after 2000 cycles at 1C, the F-NVP/C-1000 electrode can retain a high reversible capacity of 60.8 mAh g^{-1} with a favorable capacity retention of 69.3 %, while the capacity of the R-NVP/C-800 electrode rapidly decays after

600 cycles, and is negligible after 2000 cycles. The high cyclic stability observed in F-NVP/C-1000 can be the result of the stabilizing influence of the combined amorphous and crystalline states on the structural stress variations induced by the fast Na^+ insertion and extraction [55]. The sharp contrast highlights the greatly enhanced structural stability of F-NVP/C-1000 constructed by FJH technology, where the compact combination with flash graphene and the small particle dimension effectively alleviates the volume fluctuation of NVP during cycling. Moreover, the improved electrical conductivity is also responsible to the better cycling performance. To further explore the structural stability, post morphology observations of the electrodes after suffering 2000 cycles are performed. By comparing the SEM images of the two electrodes before and after cycling (Fig. S19), it is found the morphology of the F-NVP/C-1000 electrode can be well maintained, and no obvious microcracks and particle pulverization are detected. Contrarily, the surface of the R-NVP/C-800 electrode shows many microcracks and structural breakage probably due to more larger volume fluctuation during sodiation/desodiation, which can explain the poor cycling stability of this electrode material. The electrochemical performance of the F-NVP/C-1000 electrode is also compared with the recently reported NVP materials in literatures. As listed in Table S7, the F-NVP/C-1000 electrode exhibits some advantages in rate performance, signifying its promising application potential in high-power SIBs.

Besides, to further evaluate the feasibility of F-NVP/C-1000 for practical application, a commercial hard carbon (HC) is employed to assemble F-NVP/C-1000||HC full cells and the electrochemical performance is investigated. The HC electrode exhibits a featured low-potential plateau at around 0.1 V and a high reversible capacity of 281 mAh g^{-1} at 0.1C (Fig. S20a). From the initial charge/discharge curve of the F-NVP/C-1000||HC full cell depicted in Fig. 5g, a discharge specific capacity of 91.3 mAh g^{-1} and a high working voltage plateau of 3.3 V can be discerned, resulting in a favorable energy density of 283.4 Wh kg^{-1}. As seen in the inset of Fig. 5g, the assembled full battery can light on two rows of diodes, displaying the good application possibility. The charge/discharge curves at different current densities are shown in Fig. 5h. Although increasing polarization with rising current density are emerged due to the dynamical limitation, the curves at high current densities still keep the similar profile to that at 0.1C. The ever-inclining voltage plateau would be caused by the serious polarization of the HC electrode at high current densities (Fig. S20b), which also results in the much discount rate capability of the full cell when compared with the performance of the F-NVP/C-1000 electrode in half cells. Fig. S21 displays the cycling performance of the full cell at 0.25C. The capacity retention reaches 80.4 % for the 100th cycle, suggesting a favorable couple effect between the two electrodes with super cycling performance (Fig. S20c).

In order to explore the structural evolution of NVP during the desodiation and sodiation process, an ex-situ XRD test of the F-NVP/C-1000 electrode in the first charge/discharge cycle is conducted within a voltage window of 2.2–4.0 V. The XRD patterns at different charge/discharge stages are shown in Fig. 6. It is revealed that the characteristic peaks belonging to the NVP phase retain well and no other new peaks emerge during the cycling process, indicating the electrochemical process is dominated by a solid-solution reaction mechanism [50]. It is also worthy to note that, a slight shift of the (104), (113), (024) and (300) peaks toward high 2θ degree can be observed when the electrode is charged to 3.6 V and 4.0 V. The peaks then return to the state close to that of the pristine electrode when discharged to 3.0 V, demonstrating the favorable structure reversibility for guaranteeing stable V^{3+}/V^{4+} redox reactions. The crystal cell parameters of NVP at different charge and discharge conditions are summarized in Table S8. Notably, the calculated contraction ratio of cell volume at the complete desodiation condition is only 0.9 %, which is smaller than the NVP materials that fabricated by traditional furnace sintering methods [50,56]. Such small cell volume change would be due to the smaller crystalline size and lower crystallinity of the NVP particles in F-NVP/C-1000, which is also responsible to the substantially enhanced long-term cycling stability.

4. Conclusion

In summary, a carbon-modified NVP composite (F-NVP/C-1000) with nanocrystal/amorphous phase-mingled texture is developed through a facile FJH process at 1000 °C for 60 s. The COMSOL finite element analyses well depict the thermal field distribution during the FJH process, and demonstrates the proper voltage control is critical to reduce the temperature gradient of the bed and realize good material uniformity. Benefiting from the very short sintering time and rapid cooling, the FJH treatment results in the distinctly decreased dimension of the obtained NVP particles, the richer oxygen vacancies in NVP, the thinner carbon coating and increased conductivity of F-NVP/C-1000. Moreover, the crystalline size is degraded. These merits together with the nanocrystal/amorphous phase-mingled texture of NVP contribute to more pseudocapacitive charge storage behaviors and accelerated e^-/ion transportation kinetics. Therefore, the F-NVP/C-1000 electrode exhibits significantly elevated rate capability of 65.6 mAh g^{-1} at 40C and superior long-term cycling stability with a high capacity retention of 69.3 % after 2000 cycles at 1C. The full-cell performance is also favorable, demonstrating the good feasibility of FJH technologies for developing

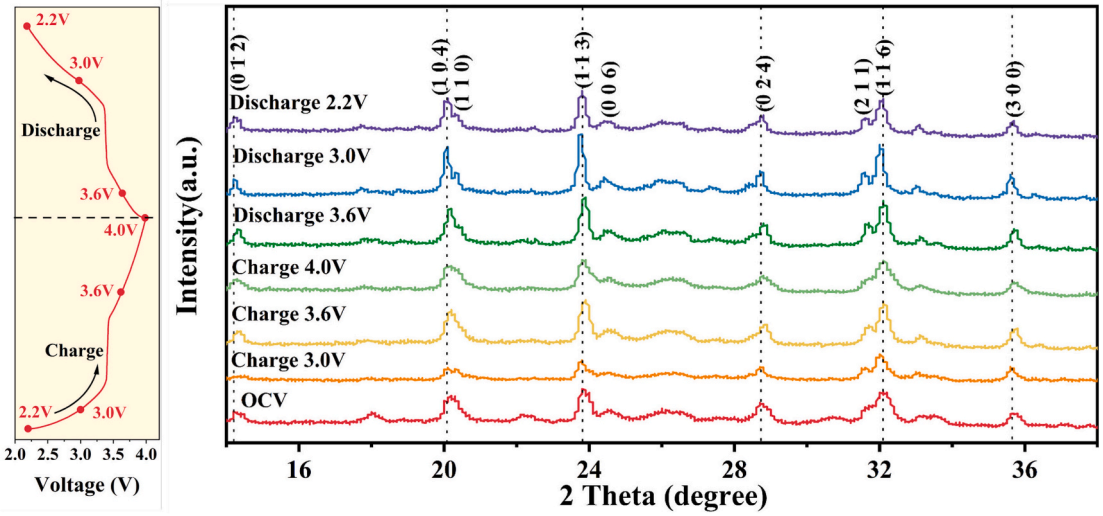

Fig. 6. The ex-situ XRD patterns of the F-NVP/C-1000 electrode at different charge/discharge states during the first cycle.

high-performance cathode materials in rechargeable batteries.

CRediT authorship contribution statement

Liying Hao: Visualization, Validation, Software, Data curation. **Zhikai Li:** Writing – original draft, Supervision, Investigation. **Lijuan Cao:** Resources. **Haigang Lv:** Supervision, Resources, Methodology. **Yun Zhao:** Writing – review & editing, Writing – original draft, Supervision, Methodology.

Declaration of competing interest

The authors declare that they have no known competing financial interests or personal relationships that could have appeared to influence the work reported in this paper.

Acknowledgements

This work was financially supported by research project from Shanxi-Zheda Institute of Advanced Materials and Chemical Engineering [No. 2022SX-TD028] and the Shanxi Provincial Key Research and Development Project (202202040201005).

Appendix A. Supplementary data

Supplementary data to this article can be found online at https://doi.org/10.1016/j.est.2025.115378.

Data availability

Data will be made available on request.

References

[1] Z.L. Chu, C.B. Yue, Core-shell structured $Na_3V_2(PO_4)_3$/C nanocrystals embedded in multi-walled carbon nanotubes: a high-performance cathode for sodium-ion batteries, Solid State Ion. 287 (2016) 36–41, https://doi.org/10.1016/j.ssi.2015.07.024.

[2] S. Dong, Y.L. Song, Y.Z. Fang, G.L. Wang, Y.Y. Gao, K. Zhu, D.X. Cao, Rapid carbonization of anthracite coal via flash joule heating for sodium ion storage, ACS Appl. Energ. Mater. 9 (2024), https://doi.org/10.1021/acsaem.3c02975.

[3] X.H. Zhang, G.Y. Han, S. Zhu, Flash nitrogen-doped carbon nanotubes for energy storage and conversion, Small 20 (3) (2024) 9, https://doi.org/10.1002/smll.202305406.

[4] L. Li, N. Zhang, Y.Q. Su, J. Zhao, Z.X. Song, D. Qian, H. Wu, M. Tahir, A.L. Saeed, S. J. Ding, Fluorine dissolution-induced capacity degradation for fluorophosphate-based cathode materials, ACS Appl. Mater. Interfaces 13 (20) (2021) 23787–23793, https://doi.org/10.1021/acsami.1c04647.

[5] H. Yu, X.P. Ruan, J.J. Wang, Z.Y. Gu, Q.H. Liang, J.M. Cao, J.Z. Kang, C.F. Du, X. L. Wu, From solid-solution MXene to Cr-substituted $Na_3V_2(PO_4)_3$: breaking the symmetry of sodium ions for high-voltage and ultrahigh-rate cathode performance, ACS Nano 12 (2022), https://doi.org/10.1021/acsnano.2c09122.

[6] Y. Yang, Y. Ma, X.J. Wang, Z.C. Gao, J.G. Yu, T. Liu, In-situ evolution of CoS/C hollow nanocubes from metal-organic frameworks for sodium-ion hybrid capacitors, Chem. Eng. J. 455 (2023) 9, https://doi.org/10.1016/j.cej.2022.140610.

[7] K. Yousefipour, R. Sarraf-Mamoory, A. Yourdkhani, Supercapacitive properties of nickel molybdate/rGO hybrids prepared by the hydrothermal method, Surf. Interfaces 29 (2022) 101638, https://doi.org/10.1016/j.surfin.2021.101638.

[8] S. Sun, Y. Chen, Q. Bai, Z. Tian, Q. Huang, C. Liu, S. He, Y. Yang, Y. Wang, L. Guo, Unravelling the regulation mechanism of nanoflower shaped $Na_3V_2(PO_4)_3$ in methanol-water system for high performance sodium ion batteries, Chem. Eng. J. 451 (2023) 138780, https://doi.org/10.1016/j.cej.2022.138780.

[9] S. Sun, S. Liu, Y. Chen, L. Li, Q. Bai, Z. Tian, Q. Huang, Y. Wang, X. Wang, L. Guo, Quantum physics and deep learning to reveal multiple dimensional modified regulation by ternary substitution of iron, manganese, and cobalt on $Na_3V_2(PO_4)_3$ for superior sodium storage, Adv. Funct. Mater. 33 (21) (2023) 2213711, https://doi.org/10.1002/adfm.202213711.

[10] L. Wang, Y. Zhao, Y. Chang, S. Zhu, X. Qi, Carbon nanotube interweaved Fe_7Se_8 nanosheet/nanorod hybrids on expanded graphite for high-performance sodium storage, J. Energy Storage 95 (2024) 112593, https://doi.org/10.1016/j.est.2024.112593.

[11] H. Zhang, L. Wang, L.L. Ma, Y.H. Liu, B.X. Hou, N.Z. Shang, S.H. Zhang, J.J. Song, S.Q. Chen, X.X. Zhao, Surface crystal modification of $Na_3V_2(PO_4)_3$ to cast intermediate $Na_2V_2(PO_4)_3$ phase toward high-rate sodium storage, Adv. Sci. 11 (3) (2024) 12, https://doi.org/10.1002/advs.202306168.

[12] Z. Yi, J. Xu, Z. Xu, M. Zhang, Y. He, J. Bao, X. Zhou, Ultrafine SnSSe/multilayer graphene nanosheet nanocomposite as a high-performance anode material for potassium-ion half/full batteries, J. Energy Chem. 60 (2021) 241–248, https://doi.org/10.1016/j.jechem.2021.01.022.

[13] Q.C. Wang, Y.J. Zhao, J.J. Gao, H.Y. Geng, J.B. Li, H.B. Jin, Triggering the reversible reaction of $V^{3+}/V^{4+}/V^{5+}$ in $Na_3V_2(PO_4)_3$ by Cr^{3+} substitution, ACS Appl. Mater. Interfaces 12 (45) (2020) 50315–50323, https://doi.org/10.1021/acsami.0c11975.

[14] E. Gu, S. Liu, Z. Zhang, Y. Fang, X. Zhou, J. Bao, An efficient sodium-ion battery consisting of reduced graphene oxide bonded $Na_3V_2(PO_4)_3$ in a composite carbon network, J. Alloy. Compd. 767 (2018) 131–140, https://doi.org/10.1016/j.jallcom.2018.07.082.

[15] E. Gu, J. Xu, Y. Du, X. Ge, X. Zhu, J. Bao, X. Zhou, Understanding the influence of different carbon matrix on the electrochemical performance of $Na_3V_2(PO_4)_3$ cathode for sodium-ion batteries, J. Alloy. Compd. 788 (2019) 240–247, https://doi.org/10.1016/j.jallcom.2019.02.202.

[16] J. Xu, E. Gu, Z. Zhang, Z. Xu, Y. Xu, Y. Du, X. Zhu, X. Zhou, Fabrication of porous $Na_3V_2(PO_4)_3$/reduced graphene oxide hollow spheres with enhanced sodium storage performance, J. Colloid Interface Sci. 567 (2020) 84–91, https://doi.org/10.1016/j.jcis.2020.01.121.

[17] Y. Jiang, Z. Yang, W. Li, L. Zeng, F. Pan, M. Wang, X. Wei, G. Hu, L. Gu, Y. Yu, Nanoconfined carbon-coated $Na_3V_2(PO_4)_3$ particles in mesoporous carbon enabling ultralong cycle life for sodium-ion batteries, Adv. Energy Mater. 5 (10) (2015) 1402104, https://doi.org/10.1002/aenm.201402104.

[18] V. Augustyn, J. Come, M.A. Lowe, J.W. Kim, P.L. Taberna, S.H. Tolbert, H. D. Abruña, P. Simon, B. Dunn, High-rate electrochemical energy storage through Li^+ intercalation pseudocapacitance, Nat. Mater. 12 (6) (2013) 518–522, https://doi.org/10.1038/nmat3601.

[19] H.B. Li, M.H. Yu, F.X. Wang, P. Liu, Y. Liang, J. Xiao, C.X. Wang, Y.X. Tong, G. W. Yang, Amorphous nickel hydroxide nanospheres with ultrahigh capacitance and energy density as electrochemical pseudocapacitor materials, Nat. Commun. 4 (2013) 7, https://doi.org/10.1038/ncomms2932.

[20] A. Van der Ven, J. Bhattacharya, A.A. Belak, Understanding Li diffusion in Li-intercalation compounds, Acc. Chem. Res. 46 (5) (2013) 1216–1225, https://doi.org/10.1021/ar200329r.

[21] J.W. Li, X.X. Cao, A.Q. Pan, Y.L. Zhao, H.L. Yang, G.Z. Cao, S.Q. Liang, Nanoflake-assembled three-dimensional $Na_3V_2(PO_4)_3$/C cathode for high performance sodium ion batteries, Chem. Eng. J. 335 (2018) 301–308, https://doi.org/10.1016/j.cej.2017.10.164.

[22] D.X. Luong, K.V. Bets, W.A. Algozeeb, M.G. Stanford, C. Kittrell, W. Chen, R. V. Salvatierra, M.Q. Ren, E.A. McHugh, P.A. Advincula, Z. Wang, M. Bhatt, H. Guo, V. Mancevski, R. Shahsavari, B.I. Yakobson, J.M. Tour, Gram-scale bottom-up flash graphene synthesis, Nature 577 (7792) (2020) 647–651, https://doi.org/10.1038/s41586-020-1938-0.

[23] C.Y. Li, Z.J. Wang, M.D. Liu, E.Z. Wang, B.L. Wang, L.L. Xu, K.L. Jiang, S.S. Fan, Y. H. Sun, J. Li, K. Liu, Ultrafast self-heating synthesis of robust heterogeneous nanocarbides for high current density hydrogen evolution reaction, Nat. Commun. 13 (1) (2022) 11, https://doi.org/10.1038/s41467-022-31077-x.

[24] P. Shen, J. Zhao, Y. Gao, Y. Lin, Y. Han, K. Xu, General synthesis of transition metal nitride arrays by ultrafast flash joule heating within 500 ms, Sci. China Chem. (2024) 1–7, https://doi.org/10.1007/s11426-023-1886-7.

[25] B. Deng, D.X. Luong, Z. Wang, C. Kittrell, E.A. McHugh, J.M. Tour, Urban mining by flash joule heating, Nat. Commun. 12 (1) (2021) 8, https://doi.org/10.1038/s41467-021-26038-9.

[26] S. Wang, Q. Liu, S. Li, F. Huang, H. Zhang, Joule-heating-driven synthesis of a honeycomb-like porous carbon nanofiber/high entropy alloy composite as an ultralightweight electromagnetic wave absorber, ACS Nano 18 (6) (2024) 5040–5050, https://doi.org/10.1021/acsnano.3c11408.

[27] Q.L. Wu, Y.H. Kang, G.H. Chen, J.K. Chen, M.H. Chen, W. Li, Z.H. Lv, H.Y. Yang, P. X. Lin, Y. Qiao, J.B. Zhao, Y. Yang, Ultrafast carbothermal shock synthesis of Wadsley-Roth phase niobium-based oxides for fast-charging lithium-ion batteries, Adv. Funct. Mater. 34 (23) (2024) 12, https://doi.org/10.1002/adfm.202315248.

[28] Z. Song, Y. Liu, Z. Guo, Z. Liu, Z. Li, J. Zhou, W. Liu, R. Liu, J. Zhang, J. Luo, Ultrafast synthesis of large-sized and conductive $Na_3V_2(PO_4)_2F_3$ simultaneously approaches high tap density, rate and cycling capability, Adv. Funct. Mater. 34 (18) (2024) 2313998, https://doi.org/10.1002/adfm.202313998.

[29] Y. Zhao, Y. Zhang, Y. Li, C. Ma, X. Qi, G. Han, Dual-complexing agent dominated synthesis of carbon coated $Na_3V_2(PO_4)_3$ cathodes for high-performance sodium ion batteries, J. Alloy. Compd. 986 (2024) 174127, https://doi.org/10.1016/j.jallcom.2024.174127.

[30] G.B. Qin, S.D. Sun, X.H. Zhang, Z. Han, Y.P. Li, G.Y. Han, Y. Li, S. Zhu, Millisecond activity modulation of atomically-dispersed Fe-N-C catalysts, Energy Storage Mater. 69 (2024) 8, https://doi.org/10.1016/j.ensm.2024.103421.

[31] L. Wang, S. Zhu, Z. Huang, M. Li, Y. Zhao, G. Han, Y. Li, J. Ni, Rapid and up-scalable flash fabrication of graphitic carbon nanocages for robust potassium storage, Adv. Funct. Mater. 2401548 (2024), https://doi.org/10.1002/adfm.202401548.

[32] Y. Chen, Z. Tian, J. Li, T. Zhou, In-situ constructing pearl necklace-shaped heterostructure: Zn^{2+} substituted $Na_3V_2(PO_4)_3$ attached on carbon nano fibers with high performance for half and full Na ion cells, Chem. Eng. J. 472 (2023) 145041, https://doi.org/10.1016/j.cej.2023.145041.

[33] Y.T. Liao, R.T. Zhu, W.J. Zhang, H.Y. Zhu, Y. Sun, J.L. Chen, Z.H. Dong, R.H. Lv, Transient synthesis of carbon-supported high-entropy alloy sulfide nanoparticles via flash joule heating for efficient electrocatalytic hydrogen evolution, Nano Res. 17 (4) (2024) 3379–3389, https://doi.org/10.1007/s12274-023-6215-8.

[34] H. Zhao, C. Hu, H. Cheng, J. Fang, Y. Xie, W. Fang, T. Doan, T. Hoang, J. Xu, P. Chen, Novel rechargeable $M_3V_2(PO_4)_3$//zinc (M= Li, Na) hybrid aqueous batteries with excellent cycling performance, Sci. Rep. 6 (1) (2016) 25809, https://doi.org/10.1038/srep25809.

[35] R.S. Kate, K. Bhattacharjee, M.V. Kulkarni, B.B. Kale, R.J. Deokate, R.S. Kalubarme, Microstructure tuned $Na_3V_2(PO_4)_3$@C electrodes toward ultra-long-life sodium-ion batteries, RSC Adv. 14 (34) (2024) 25062–25070, https://doi.org/10.1039/d4ra04221b.

[36] L.N. Zhao, H.L. Zhao, Z.H. Du, J. Wang, X.Y. Long, Z.L. Li, K. Swierczek, Delicate lattice modulation enables superior Na storage performance of $Na_3V_2(PO_4)_3$ as both an anode and cathode material for sodium-ion batteries: understanding the role of calcium substitution for vanadium, J. Mater. Chem. A 7 (16) (2019) 9807–9814, https://doi.org/10.1039/c9ta00869a.

[37] X.T. Zhang, H.L. Tian, Y.J. Cai, L. Wang, X. Yao, Z. Su, Effects of nitrogen and sulfur atom regulation on electrochemical properties of $Na_3V_2(PO_4)_2F_3$ cathode material for Na-ion batteries, Ceram. Int. 48 (24) (2022) 36129–36135, https://doi.org/10.1016/j.ceramint.2022.08.167.

[38] G. Silversmit, D. Depla, H. Poelman, G.B. Marin, R. De Gryse, Determination of the V2p XPS binding energies for different vanadium oxidation states (V^{5+} to V^{0+}), J. Electron Spectrosc. Relat. Phenom. 135 (2–3) (2004) 167–175, https://doi.org/10.1016/j.elspec.2004.03.004.

[39] J. Li, Y. Chen, S. He, Y. Yang, C. Zheng, Y. Wang, L. Guo, In-situ synthesis of porous $Na_3V_2(PO_4)_3$ with stable VOC bridge bonding by hard template method, J. Colloid Interface Sci. 650 (2023) 1476–1489, https://doi.org/10.1016/j.jcis.2023.07.113.

[40] K. Fang, H. Zhang, P. Chen, H.Y. Zhang, Z. Wei, L. Ding, X.A. Ye, J.W. Liu, Y.L. Liu, G.G. Wang, H.Y. Yang, Synergistic structure engineering and electrochemical activation modulating vanadium oxide cathode toward superior zinc-ion storage, Chem. Eng. J. 496 (2024) 11, https://doi.org/10.1016/j.cej.2024.153736.

[41] T. Zhou, Y.J. Chen, Amylopectin induces chain porous carbon skeleton boosting high performance of $Na_3V_2(PO_4)_3$, Carbon 225 (2024) 16, https://doi.org/10.1016/j.carbon.2024.119141.

[42] Q. Wang, H. Li, R. Zhang, Z. Liu, H. Deng, W. Cen, Y. Yan, Y. Chen, Oxygen vacancies boosted fast Mg^{2+} migration in solids at room temperature, Energy Storage Mater. 51 (2022) 630–637, https://doi.org/10.1016/j.ensm.2022.07.012.

[43] Y.P. Wang, K.J. Zhao, K. Wang, H.H. Li, H.B. Jiang, L. Chen, N-doped carbon confined $Na_3V_2(PO_4)_3$ derived from an organophosphonic acid as a high-performance cathode for sodium-ion batteries, J. Alloy. Compd. 844 (2020) 8, https://doi.org/10.1016/j.jallcom.2020.156118.

[44] Z.Y. Wang, J.M. Liu, Z.J. Du, H.Z. Tao, Y.Z. Yue, Enhancing Na-ion storage in $Na_3V_2(PO_4)_3$/C cathodes for sodium ion batteries through Br and N co-doping, Inorg. Chem. Front. 7 (5) (2020) 1289–1297, https://doi.org/10.1039/c9qi01690b.

[45] M. Song, Z. Yi, R. Xu, J. Chen, J. Cheng, Z. Wang, Q. Liu, Q. Guo, L. Xie, C. Chen, Towards enhanced sodium storage of hard carbon anodes: regulating the oxygen content in precursor by low-temperature hydrogen reduction, Energy Storage Mater. 51 (2022) 620–629, https://doi.org/10.1016/j.ensm.2022.07.005.

[46] C. Cai, Y. Chen, P. Hu, T. Zhu, X. Li, Q. Yu, L. Zhou, X. Yang, L. Mai, Regulating the interlayer spacings of hard carbon nanofibers enables enhanced pore filling sodium storage, Small 18 (6) (2022) 2105303, https://doi.org/10.1002/smll.202105303.

[47] H.B. Huang, S.H. Luo, C.L. Liu, Y. Yang, Y.C. Zhai, L.J. Chang, M.Q. Li, Double-carbon coated $Na_3V_2(PO_4)_3$ as a superior cathode material for Na-ion batteries, Appl. Surf. Sci. 487 (2019) 1159–1166, https://doi.org/10.1016/j.apsusc.2019.05.224.

[48] Y. Zhou, X. Yang, M. Hou, L. Zhao, X. Zhang, F. Liang, Manipulating amorphous and crystalline hybridization of $Na_3V_2(PO_4)_3$/C for enhancing sodium-ion diffusion kinetics, J. Colloid Interface Sci. 667 (2024) 64–72, https://doi.org/10.1016/j.jcis.2024.04.046.

[49] S. Nara, T. Komiya, Studies on the relationship between water-satured state and crystallinity by the diffraction method for moistened potato starch, Starch 35 (12) (1983) 407–410, https://doi.org/10.1002/star.19830351202.

[50] Z. Jian, W. Han, X. Lu, H. Yang, Y.S. Hu, J. Zhou, Z. Zhou, J. Li, W. Chen, D. Chen, Superior electrochemical performance and storage mechanism of $Na_3V_2(PO_4)_3$ cathode for room-temperature sodium-ion batteries, Adv. Energy Mater. 3 (2) (2013) 156–160, https://doi.org/10.1002/aenm.201200558.

[51] W.C. Duan, Z.Q. Zhu, H. Li, Z. Hu, K. Zhang, F.Y. Cheng, J. Chen, $Na_3V_2(PO_4)_3$@C core-shell nanocomposites for rechargeable sodium-ion batteries, J. Mater. Chem. A 2 (23) (2014) 8668–8675, https://doi.org/10.1039/c4ta00106k.

[52] J.H. Li, Y.J. Chen, T. Zhou, H.E. Shi, Z.C. Zheng, Y.Z. Wang, L. Guo, Dual-carbon coated $Na_3V_2(PO_4)_3$ derived from reduced graphene oxide and nanocellulose with porous structure for high performance sodium-ion batteries, Appl. Surf. Sci. 610 (2023) 10, https://doi.org/10.1016/j.apsusc.2022.155553.

[53] H.Y. Ma, B.C. Zhao, J. Bai, P.Y. Wang, W.Y. Li, Y.J. Mao, X.G. Zhu, Z.G. Sheng, X. B. Zhu, Y.P. Sun, Crystallinity tuning of $Na_3V_2(PO_4)_3$: unlocking sodium storage capacity and inducing pseudocapacitance behavior, Adv. Sci. 10 (4) (2023) 9, https://doi.org/10.1002/advs.202203552.

[54] S.Q. Sun, Y.J. Chen, Q. Bai, Q. Huang, C.C. Liu, S.N. He, Y.X. Yang, Y.Z. Wang, L. Guo, Unraveling the modified regulation of ternary substitution on $Na_3V_2(PO_4)_3$ for sodium ion batteries, J. Mater. Chem. A 10 (21) (2022) 11340–11353, https://doi.org/10.1039/d2ta02647c.

[55] J. Yang, Y. Wang, W. Li, L. Wang, Y. Fan, W. Jiang, W. Luo, Y. Wang, B. Kong, C. Selomulya, H.K. Liu, S.X. Dou, D. Zhao, Amorphous TiO_2 shells: a vital elastic buffering layer on silicon nanoparticles for high-performance and safe lithium storage, Adv. Mater. 29 (48) (2017) 1700523, https://doi.org/10.1002/adma.201700523.

[56] C. Sun, Y. Zhao, Q. Ni, Z. Sun, X. Yuan, J. Li, H. Jin, Reversible multielectron redox in NASICON cathode with high energy density for low-temperature sodium-ion batteries, Energy Storage Mater. 49 (2022) 291–298, https://doi.org/10.1016/j.ensm.2022.04.025.